Chinese Physics Letters **42**, 110709 (2025) **Express Letter**

Flat-Band Lieb Electride with Emergent quantum Phase Transitions and Superconductivity

Chi Ding(丁驰)[1†], Yijie Zhu(朱怡杰)[1†], Qing Lu(鲁清)[1†], Zhongwei Zhang(张仲伟)[1], Dexi Shao(邵德喜)[2], Tianheng Huang(黄天衡)[1], Yu Han(韩瑜)[1], Junjie Wang(王俊杰)[1], and Jian Sun(孙建)[1*]

[1]*National Laboratory of Solid State Microstructures, School of Physics and Collaborative Innovation Center of Advanced Microstructures, Nanjing University, Nanjing 210093, China*
[2]*School of Physics, Hangzhou Normal University, Hangzhou 311121, China*

(Received 26 August 2025; accepted manuscript online 25 September 2025)

The Lieb lattice, characterized by its distinctive Dirac cone and flat-band electronic structures, hosts a variety of exotic physical phenomena. However, its realization remains largely confined to artificial lattices. In this work, we propose the concept of a Lieb electride, where the non-bound electrons gather at the middle edges, behaving as the quasi-atoms of a Lieb lattice, enabling the emergence of flat bands. Using crystal structure prediction method MAGUS and first-principles calculations, we predict a stable candidate, Ca_2I, at ambient pressure. Distinct from conventional electrides with localized electrons at cavity centers, Ca_2I features interstitial electrons situated at cavity edges. The resultant flat bands lie close to the Fermi level, giving rise to a pronounced peak in the density of states and leading to Stoner-type ferromagnetism. With increasing pressures, we observe quantum phase transitions from ferromagnetic to non-magnetic and finally to antiferromagnetic orders in Ca_2I. Intriguingly, superconductivity emerges in the antiferromagnetic region, suggesting potential competition between these correlated states. Our study not only extends the concepts of electrides but also provides a novel strategy for realizing Lieb lattices through non-bound electrons. This work establishes Ca_2I as a promising platform for exploring flat-band physics and correlated electronic states, opening avenues for novel quantum phenomena in electride-based materials.

DOI: 10.1088/0256-307X/42/11/110709 CSTR: 32039.14.0256-307X.42.11.110709

1. Introduction. Flat bands and their induced electron correlations are one of the important aspects of condensed matter physics.[1] While complex strongly correlated systems have been extensively investigated, growing attention is now being directed toward simpler systems that nevertheless exhibit nontrivial emergent correlations and quantum phenomena.[2–4] A prominent example is the Kagome lattice, which hosts Dirac cones, flat bands, and van Hove singularities,[5] affording quantum spin liquids,[6] quantum anomalous Hall effect,[7] and charge density waves (CDWs).[8,9]

Analogous to the Kagome lattice, the Lieb lattice,[10] with a two-dimensional square lattice composed of one corner and two edge atoms, also exhibits unique geometry-frustration features. Its electronic structure is characterized by a Dirac cone intersected by a flat band, known as the Dirac-flat band. The Lieb lattice has been revealed to host a range of exotic properties, including flat-band ferromagnetism,[11,12] the fractional quantum Hall effect,[13–17] and superconductivity.[18] However, its realization in real materials remains elusive. Recent efforts have succeeded in constructing artificial Lieb lattices using engineered superlattices,[19] photonic crystals,[20–25] metal substrates,[26–29] and certain organic frameworks,[30,31] successfully replicating the Dirac-flat band structures. Nevertheless, searching for inorganic materials with intrinsic Lieb lattice geometry and well-isolated flat bands at the Fermi level continues to pose a significant challenge, limiting both the exploration of associated novel quantum phenomena and progress toward potential applications.

Electrides, a unique class of materials characterized by interstitial anionic electrons (IAEs),[32–35] have attracted increasing attention in recent years.[36–41] These IAEs impart electrides with distinctive charge distributions and various applications,[42–44] many of which also exhibit remarkable properties such as non-trivial band topology, superconductivity, and magnetism.[45–49] For instance, Gd_2C exhibits IAE-mediated ferromagnetism,[50] while $K(NH_3)_2$ undergoes spin-Peierls transitions through antiferromagnetic (AFM) IAEs.[51] These examples underscore the potential of electrides as an ideal platform for exploring electron correlations, particularly through the interactions between IAEs and lattices.

Although the interstitial cavities can conceptually be regarded as interstitial quasi-atoms (ISQs), the extent to which these ISQs emulate the behavior of real

†These authors contributed equally to this work.
*Corresponding author. Email: jiansun@nju.edu.cn

atoms remains an open and intriguing question. Particularly noteworthy is the recently proposed and experimentally realized Kagome electride in Li_5Si, where ISQs arrange into a Kagome-like network,[52] giving rise to a flat band, along with superconductivity and CDW behavior—phenomena typically associated with real Kagome materials such as CsV_3Sb_5.[53,54] The Wigner crystal might also be considered as a 2D electride emerging on a positive background.[55] Given the flat-band physics and correlation effects observed in these electrides, it is plausible that other exotic lattice geometries, such as the Lieb lattice, could also be engineered through ISQs within appropriately designed electride frameworks.

It is well established that alkaline-earth metals are highly susceptible to the accumulation of excess electrons at interstices, facilitating the formation of electrides.[56–59] In this work, we employed the crystal structure prediction method, MAGUS,[60–62] for calcium halides. We identified that the tetragonal Ca_2I exhibits electride characteristics, in which IAEs occupy 2*c* Wyckoff positions, i.e., the middle of the edge, analogous to the edge atoms in a Lieb lattice. Such arrangements of the electrides lead to 2D flat bands with several van Hove singularities, thus providing a good example for Lieb electrides. Interestingly, the strong correlations in Ca_2I trigger several quantum phase transitions from ferromagnetic (FM) to non-magnetic (NM) and then to AFM orders. Moreover, there might exist a competition between superconducting and AFM orders.

2. Methods. We employed density functional theory (DFT) within the generalized gradient approximation as implemented in the Vienna *ab initio* simulation package (VASP)[63] for structural optimization and electronic properties calculations. Convergence criteria for the forces and energy per atom were set at 0.003 eV/Å and 1×10^{-5} eV, respectively. The electron–electron exchange-correlation functional was modeled using the Perdew–Burke–Ernzerhof[64] parameters. To account for the weak interactions, we also employed the van der Waals dispersion of DFT-D3.[65,66] The projector-augmented-wave[67] method was employed with a plane wave cutoff at 600 eV. The Brillouin zone *k*-points were sampled through the Monkhorst-Pack[68] schema with a $9\times9\times4$ mesh, corresponding to a *k*-spacing resolution of $2\pi\times0.03$ Å^{-1}. The convergence test for the ENCUT and *k*-spacing parameters is well validated as shown in Fig. S1 of the Supplementary Materials (SM). A fine *k*-mesh of $24\times24\times12$ was used to integrate the magnetic moment and density of states (DOS) of the unit cell. Phonon spectrum calculations were performed within the finite displacement method with a $3\times3\times1$ supercell using the PHONOPY program package.[69] The structural and electronic properties were plotted through the VESTA[70] software.

The electron–phonon coupling (EPC) calculations were performed within the density functional perturbation theory[71] as implemented in the QUANTUM ESPRESSO package.[72,73] We employed the ultrasoft pseudo potentials with a plane wave basis-set cutoff at 80 Ry and charge density cutoff at 320 Ry.[74] The Brillouin zone was sampled with a $16\times16\times8$ *k*-mesh and a $4\times4\times2$ *q*-mesh.

3. Results and Discussions.

3.1. Lieb-Like Electride. Firstly, we presented the crystalline characteristics, from which we can illuminate the differences between the typical electride and the proposed Lieb electride, as illustrated in Figs. 1(a)–1(c). For Lieb electrides, ISQs occupied by IAEs behave as real atoms. In a conventional Lieb lattice, the Hamiltonian

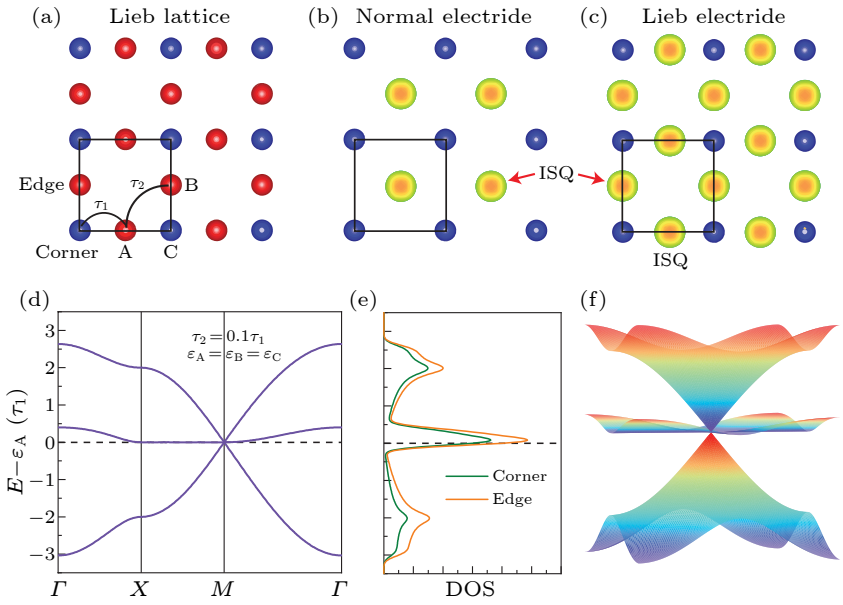

Fig. 1. Illustration of Lieb electrides. (a) Lieb lattice with corner and edge states. (b) Normal electride with IAEs at interstitial corners. (c) Lieb electrides with IAEs substituting edge atoms. (d) Simulated band structures for the tight-binding model and (e) its projected density of states into corner and edge states. (f) Band dispersions throughout the Brillouin Zone.

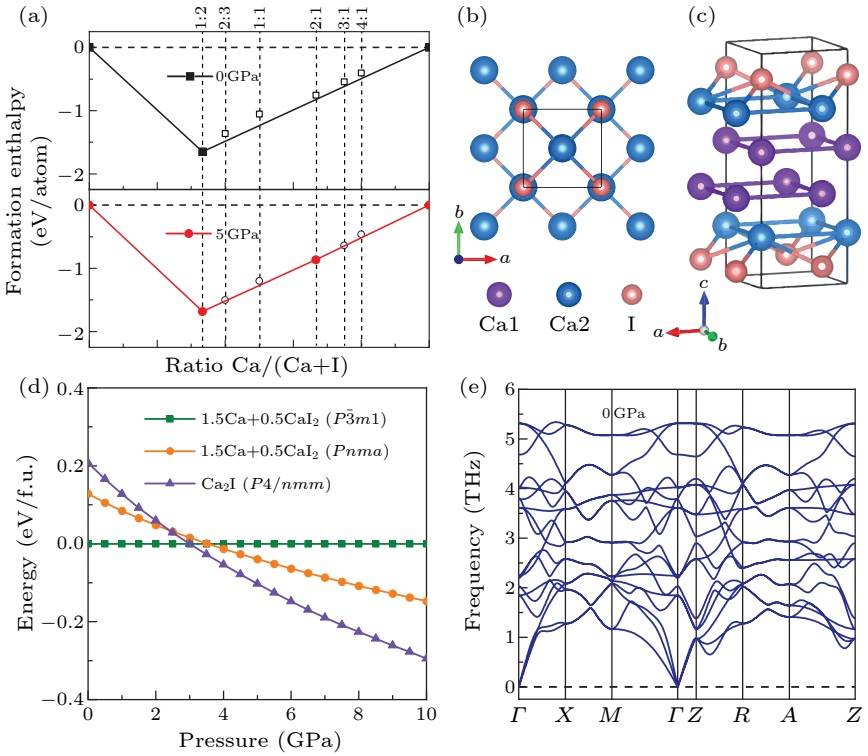

Fig. 2. Energetics and structures of Ca_2I. (a) Convex hulls at 0 GPa and 5 GPa. (b) Top view and (c) perspective view of $P4/nmm$ Ca_2I at 0 GPa. (d) Pressure-dependent enthalpy curves relative to the combination of elemental Ca and $P\bar{3}m1$ CaI_2. (e) Phonon spectrum of $P4/nmm$ Ca_2I at 0 GPa.

can be described by the following expression:

$$H = \sum_i \varepsilon_i c_i^\dagger c_i + \tau_1 \left(\sum_{\langle i,j \rangle} c_i^\dagger c_j + \text{h.c.} \right) + \tau_2 \left(\sum_{\langle\langle i,j \rangle\rangle} c_i^\dagger c_j + \text{h.c.} \right), \quad (1)$$

where ε_i represents the onsite energy for the corner and edge atoms, and τ_1 and τ_2 denote the nearest-neighbor and next-nearest-neighbor hopping terms, respectively. In an ideal tetragonal lattice with C_4 rotational symmetry, the edge atoms along the x direction (A site) and y direction (B site) are equivalent with $\varepsilon_1 = \varepsilon_2$. In this case, the band structure exhibits a perfect Dirac-flat band configuration. Distinct hopping and onsite terms not only lead to bending of the flat band but also give rise to a band gap at the Dirac point (see Fig. S2 in SM). If τ_2 is small enough, the middle flat band significantly enhances the density of states near the Fermi level, promoting strong electron correlations and enabling a range of exotic quantum phenomena.

To search for potential inorganic realizations of Lieb electrides in calcium halides, we employed the crystal structure prediction method. As a result, we found that at ambient pressure, only the CaI_2 phase is thermodynamically stable. Upon increasing pressure, one stoichiometric compound $P4/nmm$ Ca_2I becomes thermodynamically stable at 5 GPa. Its primitive cell contains two iodine atoms and four calcium atoms, which can be classified into two distinct groups, each forming two layers as shown in Fig. 2. The calculated enthalpy differences confirm that Ca_2I becomes energetically favorable above 3 GPa. Importantly, no imaginary frequencies were observed at 0 GPa, indicating that Ca_2I can be quenched to ambient pressure. Unless otherwise specified, the electronic properties discussed hereafter refer to Ca_2I at 0 GPa.

The electron localization function (ELF) reveals that IAEs, exhibiting a horseshoe-like distribution, emerge at four sites of the tetragonal unit cell as shown in Figs. 3(a) and 3(b). These IAEs are arranged into two layers that closely coincide with two Ca1 layers. For each Ca1 layer, the calcium atoms form a square lattice; however, the IAEs are not located at the centers of the squares but instead at the square edges. A cross-sectional ELF map clearly illustrates that the IAEs, with a rod-like distribution, are positioned at the edge midpoints of the calcium square lattice, thus forming a Lieb-like lattice configuration. There are two Lieb-like layers in one unit cell, stacked with a half-lattice shift along both x and y directions. The schematic illustration for the double-layer Lieb configurations for Ca_2I with the distribution of real calcium atoms and interstitial electrons is presented in Fig. S3 of the SM. Consequently, the IAEs at the A (B) sites in the top layer are vertically aligned with the B (A) sites in the bottom layer. The side view of ELF results (see Fig. S4 of the SM) indicates non-negligible wave-function overlapping and hopping terms between ISQs from two layers (Fig. S5 of the SM); therefore, the constructed tight-binding band dispersions are then presented in Fig. S6 of the SM, indicating flat band characteristics along the X–M line.

3.2. Flat-Band Properties. The Ca atoms and the

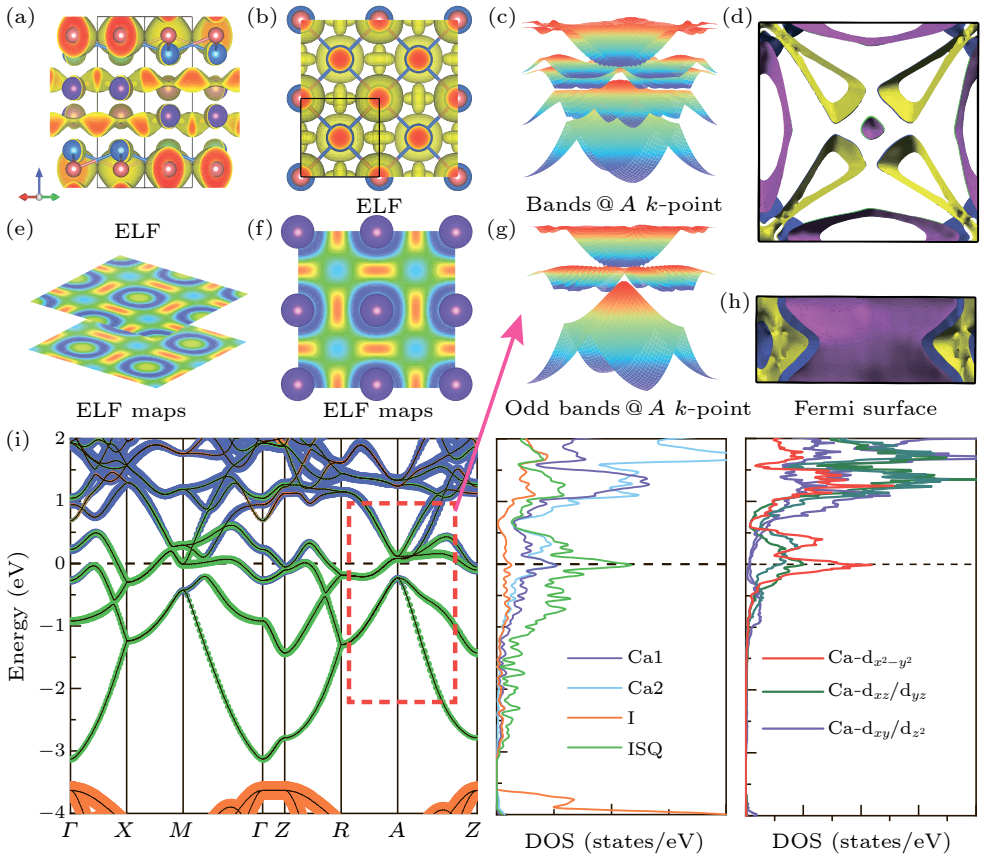

Fig. 3. Electronic properties of Ca_2I at 0 GPa. (a) Side view and (b) top view of the ELF. (c) Band dispersions for six bands across the 2D k-space around k-point A. (d) Top view of the Fermi surface. (e) Perspective of the ELF maps for two lattice planes along the [001] direction, and (f) one of them with a top view. (g) Band dispersions for three odd bands. (h) Side view of the Fermi surface. (i) Atom-projected band structures and density of states, and orbital projections for calcium atoms.

IAEs in each layer consist of the Lieb lattice. Thus, we can call the Ca_2I system a Lieb-like electride. Under the framework of the Lieb tight-binding model depicted in Eq. (1), the expected flat bands can be found in the Lieb electride Ca_2I system. Given that Ca_2I contains two Lieb-like lattices, six bands with two groups of Dirac-flat bands are expected. As shown in Fig. 3(i), six prominent bands appear in the vicinity of the Fermi level. Among them, two bands cross the Fermi level with relatively weak dispersion, while the other four exhibit strong dispersions. These six bands display likely two groups of Dirac-flat band configurations, with Dirac points being gapped. We plotted the band dispersions near point A [see Figs. 3(c) and 3(g)], where band hybridization effects are relatively weak as highlighted by dashed red lines. The band dispersions for one Dirac-flat band group in Fig. 3(g) are very close to tight-binding results in Fig. 1(f).

To elucidate the role of IAEs in the Lieb-like electride, we analyzed the atom-projected electronic band structure. As shown in Fig. 3(i), four bands near the Fermi level are predominantly derived from ISQs, while two dispersive bands above the Fermi level primarily originate from calcium atoms. The projected density of states is mainly attributed to the flat bands associated with ISQs, and then to the Ca1 atoms. It is noteworthy that Ca2 atoms, despite being far from the ISQ layers, exhibit non-negligible contributions due to their orbital hybridization with ISQs. For calcium atoms, the electronic states near the Fermi level are predominantly derived from the $d_{x^2-y^2}$ orbital, followed by a notable contribution from d_{xz} and d_{yz} orbitals. In contrast, d_{xy} and d_{z^2} orbitals contribute negligibly. For ISQs, IAEs are primarily associated with s-like orbital characteristics (see Fig. S7 of the SM).

The valence electrons of each Ca1 atom interact with four neighboring edge IAEs situated along the x and y directions, indicating that the $d_{x^2-y^2}$ orbital, whose lobes are oriented along these directions, exhibits substantial wave-function overlap with IAEs. However, due to the slight displacement of the IAEs from the Ca1 atomic plane along the z-axis, the d_{xz} and d_{yz} orbitals of Ca1 also exhibit non-negligible overlap with the IAEs. These orbital contributions are consistent with the predicted Lieb-like configuration, further supporting the formation of flat-band features arising from the specific spatial and orbital arrangement of the calcium—ISQ sublattice.

A particularly intriguing feature of the $P4/nmm$ Ca_2I structure is the appearance of IAEs at edge sites rather than at the center. Usually, the interstitial centers, with lower electron density and smaller orbital repulsion, should

be energetically more favorable for accommodating IAEs. Although the centers of the Ca1 square lattices are preferred in a purely two-dimensional framework, the presence of vertically stacked half-lattice shifted Ca2 layers introduces significant orbital repulsion, driving the IAEs to a middle position between Ca1 and Ca2 layers. Furthermore, the highly electronegative iodine atoms acquire valence electrons from calcium atoms and then exhibit a negatively charged background as confirmed by Bader charge analysis (see Table S2 of the SM). As a result, the combined electrostatic environments in Ca_2I drag IAEs toward the Ca1 atomic layers, forming a Lieb lattice configuration.

We analyzed the real-space distributions of the two flat bands, which are localized at the interstitial edges of the square lattice (Fig. S8 of the SM), thereby corroborating the above discussion. These bands display dispersion along the Γ–X and Z–R directions, particularly near the X and R points, while remaining nearly flat across other regions of the Brillouin zone, as illustrated by the band structure (Fig. 3) and its two-dimensional projection (Fig. S9 of the SM). Notably, interlayer coupling and distinct onsite energies typically destroy the flat-band characteristics of a Lieb lattice, whereas the crystalline symmetry of Ca_2I protects band degeneracy along the X–M line, in agreement with the double-layer tight-binding model (Fig. S6 of the SM). The calculated density of states further supports this finding, exhibiting a pronounced peak at the Fermi level [Fig. 3(i)]. The sharpest DOS feature has a width of approximately 0.25 eV, confirming the flat-band nature of Ca_2I.

We next compared the flat-band characteristics of Ca_2I with those of other systems. In Kagome lattices, such as CsV_3Sb_5,[8] flat bands and van Hove singularities also produce a sharp DOS peak at the Fermi level, with a peak width of about 0.2 eV, comparable to that of Ca_2I. However, Kagome lattices typically undergo CDW transitions, and the resulting electron correlation effects are challenging to address theoretically. The Kagome electride Li_5Si also shows a DOS peak near the Fermi level;[52] nevertheless, its highest DOS peak is not well isolated and remains comparable in magnitude to adjacent DOS features, indicating relatively weak electron correlations. In contrast, conventional electrides such as Ca_2N display nearly free-electron-like dispersions,[59] with little DOS variation near the Fermi level, leading to high carrier mobility but weak electronic correlations. Taken together, these comparisons highlight Ca_2I as a distinctive platform for investigating flat-band-driven phenomena.

3.3. Magnetic Phase Transformations. As discussed above, Lieb lattices are known to host a wide range of emergent physical properties, including magnetism and superconducting states. Spin-polarized calculations confirm that Ca_2I is FM, as displayed in Fig. 4(a), with a calculated total magnetic moment of 0.68 μ_B. The corresponding real-space spin density is primarily localized on the calcium atoms and then on the interstitial regions [see Fig. 4(b)], coinciding with the positions of the IAEs identified in the ELF analysis.

The observed spin splitting is predominantly concentrated near the Fermi level, within the energy window associated with the flat bands. This strongly suggests that the magnetism arises from flat-band-induced Stoner-type instabilities. The cross-sectional spin density map along the [001] direction reveals a characteristic four-lobed, flower-like distribution at the calcium sites, indicative of spin polarization from the $d_{x^2-y^2}$ orbitals, consistent with the above orbital analysis. In contrast, the ISQs exhibit a nearly spherical spin density distribution, reflecting their dominant s-orbital character. These findings motivate us to construct a simplified tight-binding Hamiltonian under bases of Ψ_s@$2c$ and $\Psi_{d_{x^2-y^2}}$@$1a$ to illuminate the essential physics in the Lieb electride of Ca_2I, including flat-band ferromagnetism and so on. The tetragonal Ca_2I is dynamically stable up to at least 30 GPa, as displayed with the non-imaginary phonon spectrum in Fig. 4(g). In the following, we investigated the evolution of magnetism under pressure. The FM moments are suppressed and decrease to zero at about 5.1 GPa, as shown in Fig. 4(f). However, when further increasing pressure, magnetism re-emerges and the magnetic moment at 30 GPa becomes larger than that at 0 GPa. More interestingly, the high-pressure phase exhibits interlayer AFM coupling between adjacent IAE layers, as illustrated in Fig. 4(e). The calculated energy differences (Fig. S10 of the SM) reveal sequential quantum phase transitions from the FM phase to the NM phase above 5.1 GPa, followed by a transition to AFM order at approximately 17.8 GPa.

To reveal the mechanism behind these transformations, we presented the pressure-dependent structural and electronic properties. The lattice parameters vary smoothly with pressure (Fig. S11 of the SM); however, the c/a ratio and the DOS at the Fermi level display three distinct regimes with two transition points, consistent with the emergence of magnetic order [Fig. 4(h)]. Since magnetism appears in both low- and high-pressure regions where the DOS at the Fermi level is enhanced, the observed spin polarization can be attributed to instabilities driven by strong electron correlations. The strong electron correlations at low pressure should give rise to a Stoner-type instability with FM order. As pressure increases, the lattice parameters c/a exhibit monotonic decreases, indicating that Ca_2I is more compressed along the z-axis. Notably, starting from 20 GPa, the absolute value of the slope decreases, indicating that the system becomes less compressible along the z-axis. The reduced lattice constants and contracted interstitial sites enhance the onsite Coulomb interactions, forcing each eigenstate to be singly occupied by a spin-polarized electron. Because the two magnetic interstitial layers are in close proximity, the localized states are energetically unfavorable. According to the Pauli exclusion principle, an AFM alignment allows electrons with opposite spins to become

more delocalized, thereby lowering the total energy compared with the FM configuration under extreme pressures. Moreover, we presented the band structure and density of states of the AFM order; the pronounced DOS peak at the Fermi level in the NM state is split and shifted to either side of the Fermi level in the AFM state (see Fig. S13 of the SM). This behavior closely resembles a Mott-type mechanism for metal–insulator transition with an AFM ground state.

3.4. Superconductivity. It is noteworthy that the high DOS near the Fermi level not only drives magnetic instability but also might introduce a superconducting gap. Within the framework of conventional BCS theory, the calculated EPC constant λ reaches approximately 0.5 at 30 GPa, with $\omega_{\log}$ being 171 cm^{-1}, corresponding to a superconducting transition temperature (T_c) of 2.1 K [Fig. 4(g)]. Phonon-projected EPC matrix elements reveal that the primary contributions to λ arise from low-frequency zones with acoustic vibrations. It is evident that the phonon dispersions at the M and Z points exhibit apparent softening and large EPCs. At ambient pressure, the calculated λ and $\omega_{\log}$ are 0.29 and 121 cm^{-1}, respectively, which are so small that they cannot trigger superconductivity. As is well known, a high DOS near the Fermi level can enhance electron–phonon interactions, which in our case show larger values below 5 GPa and above 20 GPa. This trend is consistent with the behavior of the EPC constant, which reaches its minimum around 10 GPa, as shown in Fig. S11 of the SM. Furthermore, high pressure generally increases phonon frequencies and thereby the logarithmic average frequency $\omega_{\log}$. As a result, superconductivity only emerges above 20 GPa, in contrast to magnetism, which is solely driven by the strength of electron correlations.

Usually, the contraction of lattice constants will raise the band dispersions and drive the Lieb electride towards a conventional electride, diminishing the flat-band characteristics. This stands in the low-pressure region below 10 GPa, where pressure reduces the DOS and weakens the electron–electron correlation effects responsible for magnetism. In contrast, the resurgence of high DOS in high-pressure regions is linked to Lifshitz transitions around the X and R points (see Fig. S14 of the SM), which introduce different van Hove singularities, resulting in larger plateau areas as displayed by smaller dispersive blue regions in Fig. S9 of the SM. These singularities significantly amplify the DOS and restore correlation effects. According to McMillan's formulation, the EPC constant can be approximated as $\lambda = N(E_F)\langle I^2\rangle/(M\langle\omega^2\rangle)$, where $N(E_F)$ is the DOS at the Fermi level, M is the atomic mass, $\langle I^2\rangle$ is the Fermi-surface-averaged electron–phonon matrix element, and $\langle\omega^2\rangle$ is the average squared phonon frequency. For a given system, the latter three terms typically vary only slightly; λ is approximately proportional to $N(E_F)$. For Ca_2I compounds, magnetic instability shifts the states near the Fermi level away from it, reducing the DOS from 7.2 states/eV to 3.6 states/eV, as shown in Fig. S13 of the SM. Consequently, the EPC constant is expected to decrease by a comparable factor, leading to a significant suppression of the superconducting transition temperature. This behavior suggests that the reentrant correlated flat bands may drive a competition between antiferromagnetism and superconductivity. These findings underscore the tunability of flat-band-induced correlation effects in Lieb electrides through external control parameters, such as pressure.

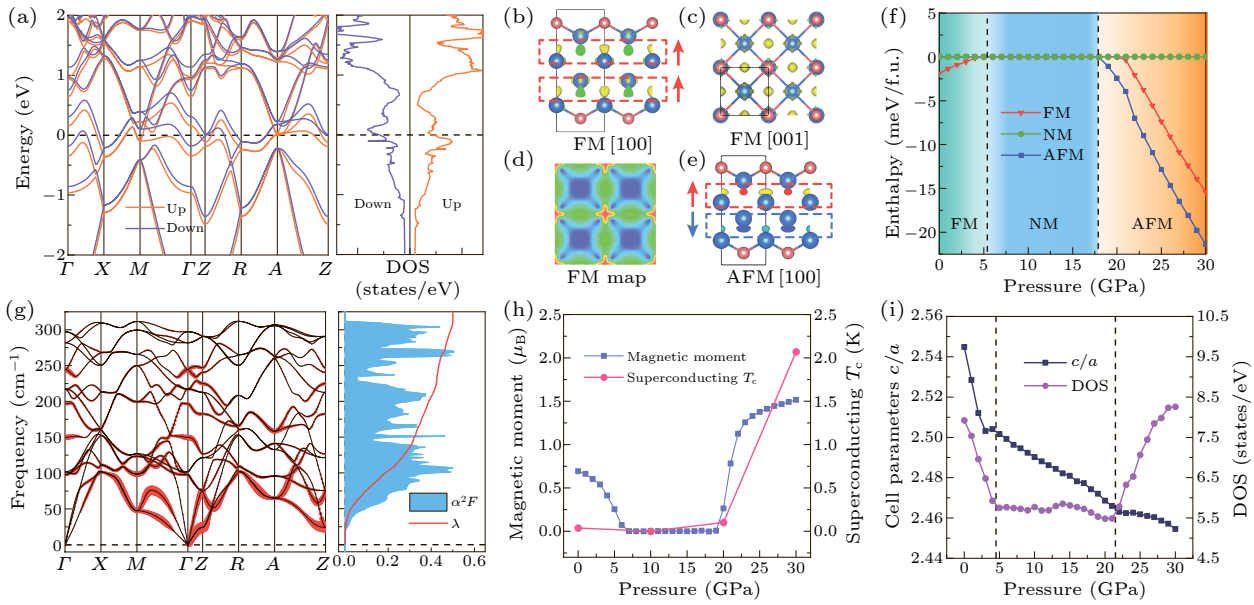

Fig. 4. Magnetic and superconducting properties. (a) Spin-polarized band structure and density of states at 0 GPa. (b) Side view and (c) top view of FM spin density at 0 GPa. (d) Spin density map along the [001] direction. (e) Side view of the AFM spin density at 30 GPa. (f) Enthalpy difference and phase diagram for NM, FM, and AFM orders. (g) EPC matrix unit decorated phonon spectrum, frequency-dependent Eliashberg function, and accumulated total EPC constant at 30 GPa. (h) Pressure-dependent superconducting T_c and magnetic moments through FM order. (i) Pressure-dependent lattice constants ratio of c/a and density of states.

4. Conclusion. In summary, we proposed the concept of Lieb electrides, where ISQs occupied by IAEs mimic the atoms of a Lieb lattice, resulting in characteristic flat bands and correlated quantum phenomena. Through crystal structure prediction method MAGUS and first-principles calculations, we identify an electride candidate, Ca_2I, at ambient pressure. The unique structure with two distinct types of calcium atomic layers with half-lattice shift facilitates the emergence of IAEs at edge sites, thereby providing a practical realization of a Lieb electride. Importantly, Ca_2I hosts flat band dispersions, and a large DOS peak at the Fermi level induces magnetism. Moreover, we reveal pressure-induced quantum phase transitions from FM to NM and ultimately to AFM orders. This AFM order should compete with superconducting states. Our findings demonstrate that ISQs can effectively emulate real atoms, extending beyond conventional Wigner crystals or Kagome lattices to other exotic configurations such as the Lieb lattice. The Ca_2I compound serves as a promising platform for exploring flat-band physics, including magnetism, superconductivity, and other correlated quantum phenomena.

Acknowledgements. This work was supported by the National Natural Science Foundation of China (Grant Nos. 12125404, T2495231, 123B2049, and 12204138), the National Key R&D Program of China (Grant No. 2022YFA1403201), the Advanced Materials-National Science and Technology Major Project (Grant No. 2024ZD0607000), the Basic Research Program of Jiangsu (Grant Nos. BK20233001 and BK20241253), the Jiangsu Funding Program for Excellent Postdoctoral Talent (Grant Nos. 2024ZB002, 2024ZB075, 2025ZB440 and 2025ZB852), the China Postdoctoral Science Foundation (Grant No. 2025M773331), the Postdoctoral Fellowship Program of CPSF (Grant No. GZC20240695 and GZC20252202), the AI & AI for Science Program of Nanjing University, Artificial Intelligence and Quantum physics (AIQ) program of Nanjing University, and the Fundamental Research Funds for the Central Universities. The calculations were carried out using supercomputers at the High Performance Computing Center of Collaborative Innovation Center of Advanced Microstructures, the high-performance supercomputing center of Nanjing University.

References

[1] Paschen S and Si Q 2021 *Nat. Rev. Phys.* **3** 9
[2] Cao Y, Rodan-Legrain D, Rubies-Bigorda O, Park J M, Watanabe K, Taniguchi T, and Jarillo-Herrero P 2020 *Nature* **583** 215
[3] Saito Y, Ge J, Watanabe K, Taniguchi T, and Young A F 2020 *Nat. Phys.* **16** 926
[4] Jaoui A, Das I, Di Battista G, Díez-Mérida J, Lu X, Watanabe K, Taniguchi T, Ishizuka H, Levitov L, and Efetov D K 2022 *Nat. Phys.* **18** 633
[5] Ye L, Kang M, Liu J, von Cube F, Wicker C R, Suzuki T, Jozwiak C, Bostwick A, Rotenberg E, Bell D C, Fu L, Comin R, and Checkelsky J G 2018 *Nature* **555** 638
[6] Balents L 2010 *Nature* **464** 199
[7] Xu G, Lian B, and Zhang S C 2015 *Phys. Rev. Lett.* **115** 186802
[8] Tan H, Liu Y, Wang Z, and Yan B 2021 *Phys. Rev. Lett.* **127** 046401
[9] Wilson S D and Ortiz B R 2024 *Nat. Rev. Mater.* **9** 420
[10] Lieb E H 1989 *Phys. Rev. Lett.* **62** 1201
[11] Tasaki H 1992 *Phys. Rev. Lett.* **69** 1608
[12] Tasaki H 1994 *Phys. Rev. Lett.* **73** 1158
[13] Weeks C and Franz M 2010 *Phys. Rev. B* **82** 085310
[14] Goldman N, Urban D F, and Bercioux D 2011 *Phys. Rev. A* **83** 063601
[15] Neupert T, Santos L, Chamon C, and Mudry C 2011 *Phys. Rev. Lett.* **106** 236804
[16] Tang E, Mei J W, and Wen X G 2011 *Phys. Rev. Lett.* **106** 236802
[17] Wang Y F, Gu Z C, Gong C D, and Sheng D N 2011 *Phys. Rev. Lett.* **107** 146803
[18] Julku A, Peotta S, Vanhala T I, Kim D H, and Törmä P 2016 *Phys. Rev. Lett.* **117** 045303
[19] Lee S, de Sousa D J P, Jalan B, and Low T 2024 *Sci. Adv.* **10** eadq0293
[20] Shen R, Shao L B, Wang B, and Xing D Y 2010 *Phys. Rev. B* **81** 041410
[21] Guzmán-Silva D, Mejía-Cortés C, Bandres M A, Rechtsman M C, Weimann S, Nolte S, Segev M, Szameit A, and Vicencio R A 2014 *New J. Phys.* **16** 063061
[22] Taie S, Ozawa H, Ichinose T, Nishio T, Nakajima S, and Takahashi Y 2015 *Sci. Adv.* **1** e1500854
[23] Vicencio R A, Cantillano C, Morales-Inostroza L, Real B, Mejía-Cortés C, Weimann S, Szameit A, and Molina M I 2015 *Phys. Rev. Lett.* **114** 245503
[24] Diebel F, Leykam D, Kroesen S, Denz C, and Desyatnikov A S 2016 *Phys. Rev. Lett.* **116** 183902
[25] Xia S, Hu Y, Song D, Zong Y, Tang L, and Chen Z 2016 *Opt. Lett.* **41** 1435
[26] Drost R, Ojanen T, Harju A, and Liljeroth P 2017 *Nat. Phys.* **13** 668
[27] Slot M R, Kempkes S N, Knol E J, van Weerdenburg W M J, van den Broeke J J, Wegner D, Vanmaekelbergh D, Khajetoorians A A, Morais Smith C, and Swart I 2019 *Phys. Rev. X* **9** 011009
[28] Yan L and Liljeroth P 2019 *Advances in Physics: X* **4** 1651672
[29] Li X, Li Q, Ji T, Yan R, Fan W, Miao B, Sun L, Chen G, Zhang W, and Ding H 2022 *Chin. Phys. Lett.* **39** 057301
[30] Jiang W, Huang H, and Liu F 2019 *Nat. Commun.* **10** 2207
[31] Cui B, Zheng X, Wang J, Liu D, Xie S, and Huang B 2020 *Nat. Commun.* **11** 66
[32] Inoshita T, Jeong S, Hamada N, and Hosono H 2014 *Phys. Rev. X* **4** 031023
[33] Park J, Lee K, Lee S Y, Nandadasa C N, Kim S, Lee K H, Lee Y H, Hosono H, Kim S G, and Kim S W 2017 *J. Am. Chem. Soc.* **139** 615
[34] Ming W, Yoon M, Du M H, Lee K, and Kim S W 2016 *J. Am. Chem. Soc.* **138** 15336
[35] Tsuji Y, Dasari P L V K, Elatresh S F, Hoffmann R, and Ashcroft N W 2016 *J. Am. Chem. Soc.* **138** 14108
[36] Dye J L 2003 *Science* **301** 607
[37] Gao J, Qian Y, Jia H, Guo Z, Fang Z, Liu M, Weng H, and Wang Z 2022 *Sci. Bull.* **67** 598
[38] Nie S, Qian Y, Gao J, Fang Z, Weng H, and Wang Z 2021 *Phys. Rev. B* **103** 205133
[39] Wang X, Wang Y, Wang J, Pan S, Lu Q, Wang H T, Xing D, and Sun J 2022 *Phys. Rev. Lett.* **129** 246403
[40] Wang Y, Wang J, Hermann A, Liu C, Gao H, Tosatti E, Wang H T, Xing D, and Sun J 2021 *Phys. Rev. X* **11** 011006
[41] Zhang Y, Wang H, Wang Y, Zhang L, and Ma Y 2017 *Phys. Rev. X* **7** 011017

[42] Kitano M, Inoue Y, Yamazaki Y, Hayashi F, Kanbara S, Matsuishi S, Yokoyama T, Kim S W, Hara M, and Hosono H 2012 *Nat. Chem.* **4** 934

[43] Hu J P, Xu B, Yang S Y A, Guan S, Ouyang C Y, and Yao Y G 2015 *ACS Appl. Mater. Interfaces* **7** 24016

[44] Hosono H, Kim J, Toda Y, Kamiya T, and Watanabe S 2017 *Proc. Natl. Acad. Sci. U. S. A.* **114** 233

[45] Liu S, Wang C, Jeon H, Kim J, and Cho J H 2022 *Phys. Rev. B* **105** L041406

[46] Zhang X, Xiao Z, Lei H, Toda Y, Matsuishi S, Kamiya T, Ueda S, and Hosono H 2014 *Chem. Mater.* **26** 6638

[47] Otani S, Hirata K, Adachi Y, and Ohashi N 2016 *J. Cryst. Growth* **454** 15

[48] Park J, Hwang J Y, Lee K H, Kim S G, Lee K, and Kim S W 2017 *J. Am. Chem. Soc.* **139** 17277

[49] Hiraishi M, Kojima K M, Yamauchi I, Okabe H, Takeshita S, Koda A, Kadono R, Zhang X, Matsuishi S, Hosono H, Hirata K, Otani S, and Ohashi N 2018 *Phys. Rev. B* **98** 041104

[50] Lee S Y, Hwang J Y, Park J, Nandadasa C N, Kim Y, Bang J, Lee K, Lee K H, Zhang Y, Ma Y, Hosono H, Lee Y H, Kim S G, and Kim S W 2020 *Nat. Commun.* **11** 1526

[51] Ding C, Lu Q, Guo Z, Huang T, Wang J, Han Y, Xing D, and Sun J 2024 *Sci. Bull.* **69** 1027

[52] You J Y, Gu B, Su G, and Feng Y P 2022 *J. Am. Chem. Soc.* **144** 5527

[53] Chen K Y, Wang N N, Yin Q W, Gu Y H, Jiang K, Tu Z J, Gong C S, Uwatoko Y, Sun J P, Lei H C, Hu J P, and Cheng J G 2021 *Phys. Rev. Lett.* **126** 247001

[54] Liang Z, Hou X, Zhang F, Ma W, Wu P, Zhang Z, Yu F, Ying J J, Jiang K, Shan L, Wang Z, and Chen X H 2021 *Phys. Rev. X* **11** 031026

[55] Fujimori A 2022 *Nat. Mater.* **21** 1217

[56] Miyakawa M, Kim S W, Hirano M, Kohama Y, Kawaji H, Atake T, Ikegami H, Kono K, and Hosono H 2007 *J. Am. Chem. Soc.* **129** 7270

[57] Liu Y X, Wang C, Han S, Chen X, Sun H R, and Liu X B 2021 *Chin. Phys. Lett.* **38** 036201

[58] Ding C, Zhang Z, Lu Q, Zhu Y, Liang Z, Wang J, and Sun J 2025 *Phys. Rev. B* **111** 104113

[59] Lee K, Kim S W, Toda Y, Matsuishi S, and Hosono H 2013 *Nature* **494** 336

[60] Xia K, Gao H, Liu C, Yuan J, Sun J, Wang H T, and Xing D 2018 *Sci. Bull.* **63** 817

[61] Wang J, Gao H, Han Y, Ding C, Pan S, Wang Y, Jia Q, Wang H T, Xing D, and Sun J 2023 *Natl. Sci. Rev.* **10** nwad128

[62] Han Y, Ding C, Wang J, Gao H, Shi J, Yu S, Jia Q, Pan S, and Sun J 2025 *Nat. Comput. Sci.* **5** 255

[63] Kresse G and Furthmuller J 1996 *Phys. Rev. B* **54** 11169

[64] Perdew J P, Burke K, and Ernzerhof M 1996 *Phys. Rev. Lett.* **77** 3865

[65] Grimme S, Antony J, Ehrlich S, and Krieg H 2010 *J. Chem. Phys.* **132** 154104

[66] Grimme S, Ehrlich S, and Goerigk L 2011 *J. Comput. Chem.* **32** 1456

[67] Blöchl P E 1994 *Phys. Rev. B* **50** 17953

[68] Monkhorst H J and Pack J D 1976 *Phys. Rev. B* **13** 5188

[69] Togo A, Oba F, and Tanaka I 2008 *Phys. Rev. B* **78** 134106

[70] Momma K and Izumi F 2011 *J. Appl. Crystallogr.* **44** 1272

[71] Baroni S, Giannozzi P, and Testa A 1987 *Phys. Rev. Lett.* **58** 1861

[72] Giannozzi P, Baroni S, Bonini N, Calandra M, Car R, Cavazzoni C, Ceresoli D, Chiarotti G L, Cococcioni M, Dabo I, Dal Corso A, de Gironcoli S, Fabris S, Fratesi G, Gebauer R, Gerstmann U, Gougoussis C, Kokalj A, Lazzeri M, Martin-Samos L, Marzari N, Mauri F, Mazzarello R, Paolini S, Pasquarello A, Paulatto L, Sbraccia C, Scandolo S, Sclauzero G, Seitsonen A P, Smogunov A, Umari P, and Wentzcovitch R M 2009 *J. Phys. Condens. Matter* **21** 395502

[73] Perdew J P and Zunger A 1981 *Phys. Rev. B* **23** 5048

[74] Vanderbilt D 1990 *Phys. Rev. B* **41** 7892